Small admixture of nonadiabaticity facilitating topologically protected splitters and routers via optimizing coupling engineering

Jia-Ning Zhang,[1] Jin-Lei Wu,[2,*] Jin-Xuan Han,[1] Shuai Tang,[1] Jie Song,[1] and Yong-Yuan Jiang[1,3,4,5,†]

[1]*School of Physics, Harbin Institute of Technology, Harbin 150001, China*
[2]*School of Physics and Laboratory of Zhongyuan Light, Zhengzhou University, Zhengzhou 450001, China*
[3]*Collaborative Innovation Center of Extreme Optics, Shanxi University, Taiyuan 030006, China*
[4]*Key Laboratory of Micro-Nano Optoelectronic Information System, Ministry of Industry and Information Technology, Harbin 150001, China*
[5]*Key Laboratory of Micro-Optics and Photonic Technology of Heilongjiang Province, Harbin Institute of Technology, Harbin 150001, China*

(Received 27 August 2023; accepted 27 February 2024; published 14 March 2024)

We propose to implement fast and robust quantum state transfer in symmetrical beam splitters and routers through a specific topological edge channel in splicing Su-Schrieffer-Heeger–like models, for which a small admixture of nonadiabatic character into evolution facilitates the accelerated adiabatic pumping process to a great extent. Through optimizing coupling engineering, we develop the acceleration capacity for the symmetrical beam splitting process, and we investigate robustness enhancement against disorders and environment-induced losses. Furthermore, the model manifests good scalability and can be extended to a crossed-chain configuration of realizing a topological router with tunable numbers of output ports. Finally, we discuss the experimentally feasible implementation in quantum optomechanical systems by alternately assembling optical cavities and mechanical oscillators, enabling topologically protected splitters and routers of photons or phonons. This work provides a typical example of a functional quantum device, which could motivate further research into efficient quantum information processing and the construction of large-scale quantum networks.

DOI: 10.1103/PhysRevB.109.094303

I. INTRODUCTION

Excitation transfers in classical and quantum networks have extensive applications in different fields, such as coherent control of chemical reactions [1], effective exciton transport in organic molecules [2,3], quantum state transfer, and large-scale quantum information processing [4,5]. A fundamental mission in the construction of large-scale quantum networks is to achieve efficient and undistorted transmission of quantum states encoded with information between different nodes [6–8]. To enhance the resilience of a quantum state transfer (QST) process to perturbation in actual physical systems and the decoherence effect induced by the environment, multiple technical solutions such as tunable coupling [9–11], quantum error correction [12–14], dark mode assistance [15], and dissipative tunneling [16] have been proposed. In addition to these conventional techniques, the discovery of topological insulators in condensed-matter physics paves the way for efficient and robust quantum information processing [17,18]. Due to the topological nonequivalence of its energy band structures in momentum space as compared with a traditional insulator, topological insulators possess insulating bulk but support conducting states at the boundary of the system simultaneously [19–22]. The conductive boundary states enable lossless and unidirectional propagation of information, which is attributed to their outstanding insensitivity to local perturbations and disorder [23,24], making them an excellent platform for high-fidelity QST [25–28], quantum computing [29,30], quantum interference [31], and quantum entanglement [32,33].

As the simplest one-dimensional lattice with nontrivial topological boundary states, the Su-Schrieffer-Heeger (SSH) model was initially abstracted from polyacetylene to study the formation of solitons in the 1980s [34], and it has been intensively exploited to describe spinless fermions hopping on a one-dimensional lattice with staggered hopping amplitudes [35–37]. Due to the simple lattice configuration of the SSH model, it can be mapped easily in various different physical systems such as optomechanical arrays [27,28,38–40], quantum dots [41–43], coupled waveguides [44–50], superconducting circuits [51–54], coupled-cavity arrays [55,56], etc., which provides broad experimental feasibility for the implementation of topologically protected quantum communication based on the SSH model. In addition, the SSH model and its generalized counterparts can hold rich forms of edge states [57–62], based on which researchers have designated numerous quantum optical devices such as topological beam splitters [63,64], topological routers [65,66], and topological lasers [67–71]. Essentially, based on robust excitation transfer via adiabatic evolution of the topological channel states, these devices generally require a long duration of evolution for successful QST so as to limit their practical applications. However, existing methods for fast topological pumping

*jlwu517@zzu.edu.cn
†jiangyy@hit.edu.cn

concentrate mainly on improving the QST efficiency in the point-to-point transmission via topologically protected edge states [50,72–76]. Therefore, it is of urgent need and great significance to accelerate QST in specific quantum optical devices based on the SSH model.

In this paper, we propose to realize efficient topologically protected QST from a central site to two ends in a symmetrical beam splitter based on a succession of two SSH chains showing distinct topological orders with staggered on-site potentials. Based on adiabatic theory and numerical analysis of the instantaneous spectrum, our approach conducts delicate modulation on the nearest-neighbor (NN) hopping as well as staggered on-site potentials using different driving functions, so that the system can be driven strongly in the case of a large energy gap between the channel and bulk states but mildly in the case of a small energy gap. Through optimization of parameters, we show that the beam splitter adopting the tangential and three-step modulation schemes that contain a small admixture of nonadiabatic character into adiabatic QST can be accelerated by up to seven and ten times, respectively, over the commonly used trigonometric counterpart. By observing the performance of the tangential and three-step protocols under diagonal and off-diagonal disorders and environmental losses, we conclude through numerical sampling that one drawback accompanying the accelerating effect for both schemes is the reduced resilience of the system to off-diagonal disorder, while at the same time the system still exhibits strong robustness against diagonal disorder and improved robustness against environment-induced losses for the tangential and three-step protocols.

Furthermore, we confirm the good scalability of the beam splitter modulated by the protocols, and we discover that the proposed model can be extended to a crossed-chain configuration to construct a topological router with an adjustable number of output ports. In addition, we also discuss experimental implementation of the protocol through constructing optomechanically coupled systems to implement topologically protected splitters and routers of photons or phonons by alternately assembling optical cavities and mechanical oscillators. Our work provides a typical example of a functional quantum device, which could induce further research into efficient quantum information processing and the construction of large-scale quantum networks.

II. PHYSICAL MODEL AND ENGINEERING OF TOPOLOGICAL PUMPING

A. Symmetrical beam splitter via edge channel in a splicing SSH model

To realize a symmetrical topological splitter, we consider here an odd-sized SSH model comprised of $L = 2N + 1$ sites, as schematically shown in Fig. 1, in which each unit cell contains two sublattice sites a_n and b_n with the staggered on-site potentials V_a and V_b. For the first half of the lattice chain, the intracell and intercell NN hopping amplitudes between two adjacent sites are J_1 and J_2, respectively, while for the second half of the lattice chain, intracell and intercell hopping amplitudes are exchanged, generating a topological interface at the site $a_{N/2+1}$. The number of unit cells N is

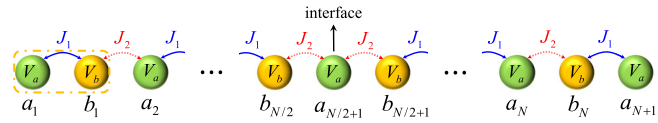

FIG. 1. Diagrammatic sketch of an odd-sized SSH model structured by interfacing two SSH chains with distinct topological orders. Each unit cell contains a pair of a- and b-type sites, as shown in the yellow dashed rounded rectangle. The size of the SSH chain is $L = 2N + 1$ (N being even). The NN hopping rates $J_{1,2}$ and staggered on-site energies $V_{a,b}$ are mirror-symmetric with respect to the topological interface.

set to be an even number, so that the topological interface falls on an a-type site. The lattice chain mentioned above can be described by the following second-quantized Hamiltonian (using the natural unit $\hbar = 1$):

$$\begin{aligned} H = &\sum_{n}^{N+1} V_a a_n^\dagger a_n + \sum_{n}^{N} V_b b_n^\dagger b_n \\ &+ \sum_{n=1}^{N/2} \left[J_1 a_n^\dagger b_n + J_2 a_{n+1}^\dagger b_n + \text{ H.c.} \right] \\ &+ \sum_{n=N/2+1}^{N} \left[J_2 a_n^\dagger b_n + J_1 a_{n+1}^\dagger b_n + \text{ H.c.} \right], \end{aligned} \tag{1}$$

where a_n ($a_n^\dagger$) and b_n ($b_n^\dagger$) are the annihilation (creation) operators of a particle at the nth a-type and b-type sites, respectively. The first term denotes on-site potentials of two types of sites, while the second and third terms represent the NN hopping amplitudes between two adjacent sites for the first and second halves of the lattice chain. For a finite-sized lattice chain, when staggered on-site potentials are imposed on the system, i.e., $V_a = -V_b$, by analytically solving the eigenvalue equation under the open boundary condition, we can find a special eigenstate with eigenenergy V_a expressed by distribution of probability amplitudes of the $2N + 1$ sites,

$$\begin{aligned} |\psi_{V_a}\rangle &= \Big| \rho_{a,1} e^{i\phi_{a,1}}, \rho_{b,1} e^{i\phi_{b,1}}, \ldots, \rho_{a,\frac{N}{2}+1} e^{i\phi_{a,\frac{N}{2}+1}}, \ldots, \\ &\quad \times \rho_{b,N} e^{i\phi_{b,N}}, \rho_{a,N+1} e^{i\phi_{a,N+1}} \Big\rangle \\ &= \left| 1, 0, \xi, 0, \xi^2, 0, \ldots, 0, \xi^{N/2}, 0, \ldots, 0, \xi^2, 0, \xi, 1 \right\rangle, \end{aligned} \tag{2}$$

where $\xi = -J_1/J_2$ denotes the decay factor of the on-site probability amplitude depending on the ratio of J_1 and J_2. Obviously, when the NN hopping configuration satisfies $J_1 > J_2$, the normalized distribution of this eigenstate is localized at the interface site, while when $J_1 < J_2$ it is localized at two end sites. Its localized position can be conveniently modulated by continuously tuning the intracell and intercell hopping amplitudes and can thus serve as a topologically protected quantum channel. When setting $J_1/J_2 = +\infty$ initially and $J_1/J_2 = 0$ finally, an excitation injected into the interface site can be transferred to two end sites with equal probabilities. If we regard the interface site as an input port, and the two end sites as output ports, then the lattice configuration illustrated in Fig. 1 is equivalent to a symmetrical beam splitter. It is

worth noting that such a symmetrical beam splitting process is topologically protected by the energy gap between the channel and its adjacent bulk states, thus the symmetrical beam splitter is immune to inherent defects and inevitable local disorders residing in the system.

B. Characteristics of driving functions and analysis of the spectrum

To realize a topologically protected QST from the interface to the two ends, it is necessary to take a glimpse of the characteristic of the NN hopping amplitudes, which can be written in the form [74]

$$J_1(t) = J^+ + J^- f(t), \quad J_2(t) = J^+ - J^- f(t), \tag{3}$$

where $J^+ = \frac{J_1(0)+J_2(0)}{2}$, $J^- = \frac{J_1(0)-J_2(0)}{2}$. To realize symmetrical beam splitting, we need continuous modulation of J_1/J_2 from $+\infty$ to 0. We can try to achieve this by dynamic control of the driving function $f(t)$ from 1 to -1, so that the intracell and intercell hopping rates exchange their values between initial and final instants, namely

$$J_1(0) = J_0, \quad J_2(0) = 0, \quad J_1(t^*) = 0, \quad J_2(t^*) = J_0. \tag{4}$$

The implementation of the beam splitting function is essentially based on adiabatic evolution of the topological channel state. To satisfy the adiabatic limit, a sufficient condition is $\sum_{m\neq n} \frac{\langle\psi_n(t)|\frac{\partial \hat{H}(t)}{\partial t}|\psi_m(t)\rangle}{|E_m(t)-E_n(t)|} \ll 1$, where E_n, E_m, $|\psi_n(t)\rangle$, $|\psi_m(t)\rangle$ are the nth and mth eigenenergies and corresponding eigenstates obeying the instantaneous eigenequation $H(t)|\psi_n(t)\rangle = E_n(t)|\psi_n(t)\rangle$. Generally, the energy gap between the channel and bulk states is quite small, thus the system should be driven slowly enough to make the initial state evolve along the channel state without exciting bulk states. To realize fast beam splitting which satisfies the adiabatic condition so as to prevent the topological channel state from leaking into the bulk states, the instantaneous energy gap between the channel and bulk states should be sufficiently large, and the differentiation of the Hamiltonian with respect to time, which is proportional to the slope of the driving function $f(t)$, should be sufficiently small. One extensively researched method to suppress nonadiabatic effects and override the adiabatic constraint of sufficiently long total evolution time needed for a successful QST is a shortcut to adiabaticity [73], in which carefully devised counter-adiabatic terms in the Hamiltonian are introduced to cancel nonadiabatic excitations. In this work, we try to enhance the speed of QST through dynamic control of the NN hopping in which the system can be driven strongly in the case of a large energy gap between the channel and bulk states and mildly in the case of a small energy gap. This approach only involves engineering of the driving function, and therefore the evolution process is always accompanied by slight nonadiabatic transition excitations.

We start our analysis with the commonly used trigonometric modulation of not only the NN hopping amplitudes but also on-site energies,

$$f(t) = \cos\left(\frac{\pi t}{t^*}\right), \tag{5a}$$

$$J_1 = \frac{J_0}{2}\left(1 + \cos\frac{\pi t}{t^*}\right), \tag{5b}$$

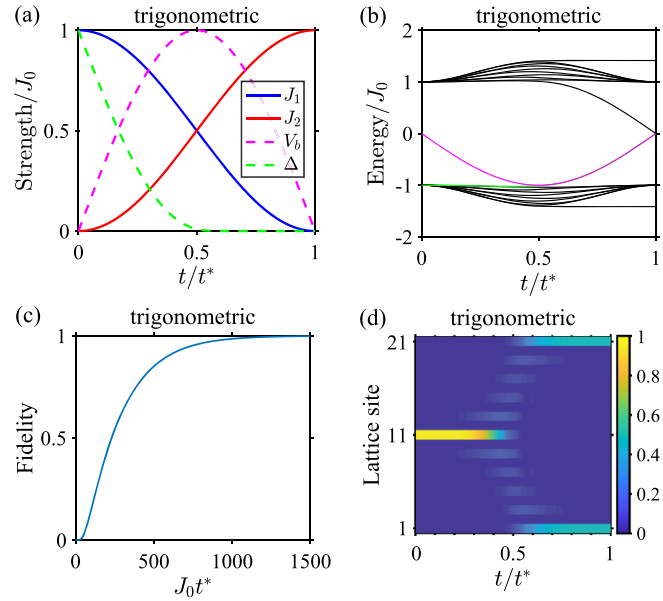

FIG. 2. (a) Dynamic control of hopping amplitudes (solid blue and red lines) and staggered on-site energies (magenta dotted line), as well as evolution of the energy gap between the gap state and the adjacent bulk state (green dotted line) for the trigonometric protocol. (b) Instantaneous energy spectrum as a function of the normalized time t/t^*. (c) Fidelity of the symmetrical topological beam splitter assisted via edge pumping vs total transfer time t*. (d) Distribution of the gap state during the evolution process. The chain is comprised of $L = 21$ sites.

$$J_2 = \frac{J_0}{2}\left(1 - \cos\frac{\pi t}{t^*}\right), \tag{5c}$$

$$V_b = -V_a = J_0\sqrt{\frac{J_2(2t)}{J_0}} = J_0 \sin\left(\frac{\pi t}{t^*}\right), \tag{5d}$$

where t^* denotes the total QST time. According to the definitions in Eqs. (5b) and (5c), $J_{1,2}$ satisfy $J_1/J_2 = +\infty$ and $J_1/J_2 = 0$ at the initial and end moments, respectively. Consequently, the system can perform a topologically protected QST from the interface site to two end sites, corresponding to a symmetrical beam splitting process. To examine how faithfully the QST process in the beam splitter has taken place, we introduce the transfer fidelity defined as $F = |\langle\Psi_t \mid \Psi(t^*)\rangle|^2$, i.e., the square of the modulus of the inner product of the target state $|\Psi_t\rangle = \frac{1}{\sqrt{2}}|1, 0, 0, \ldots, 0, 0, 0, \ldots, 0, 0, 1\rangle$ and the evolved final state $|\Psi(t^*)\rangle$ which can be obtained by numerically solving the time-dependent Schrödinger equation. The initial state of the system $|\Psi_i\rangle = |0, 0, 0, \ldots, 0, 1, 0, \ldots, 0, 0, 0\rangle$ is specified to set the interface site as the input port of the beam splitter. Without a loss of generality, taking the system with a chain length of $L = 21$ for example, we plot in Figs. 2(a)–2(d) modulation of the NN hopping amplitudes and staggered on-site energies for the trigonometric protocol, evolution of the corresponding instantaneous energy spectrum, the QST fidelity of beam splitter versus the total transfer time, and the distribution of the gap state during the QST process, respectively. Comparing the evolution of the gap states

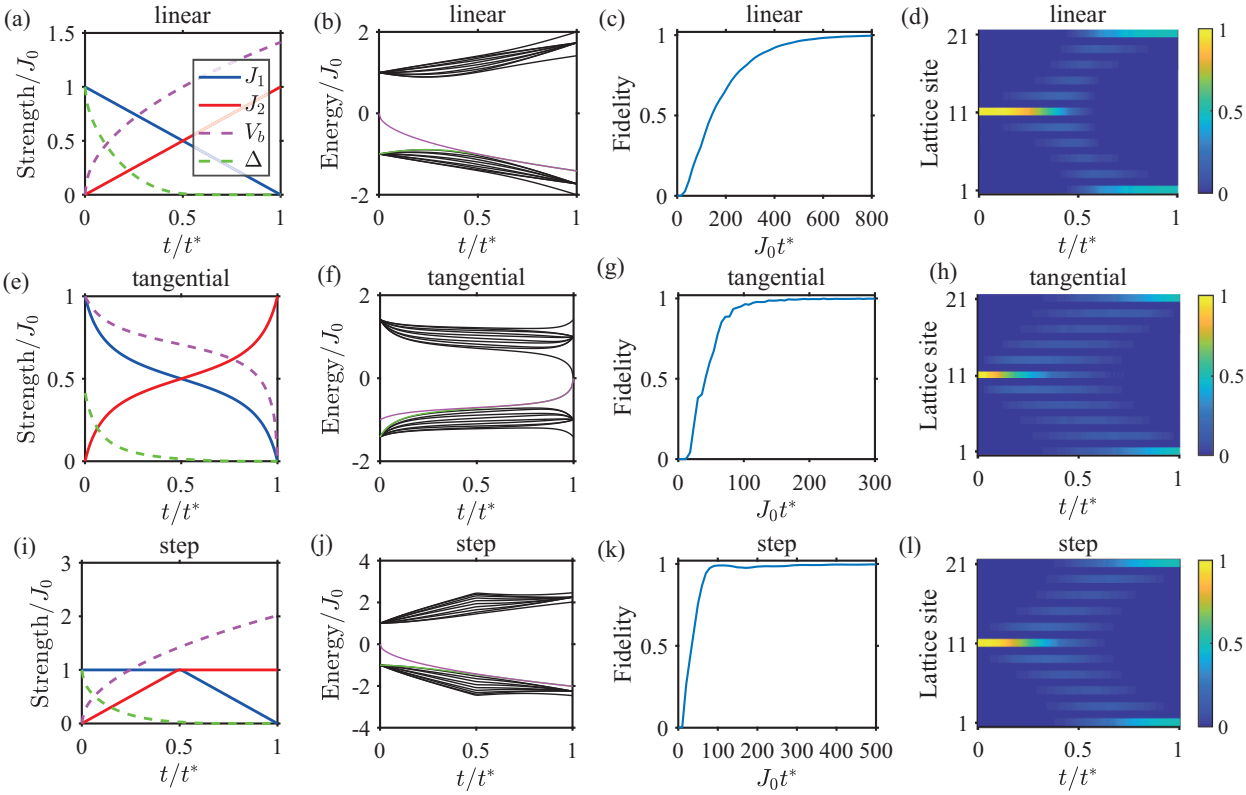

FIG. 3. (a),(e),(i) Modulation of hopping amplitudes and staggered on-site energy, as well as evolution of energy gap between the gap state and the adjacent bulk state for the linear protocol in (a), for the tangential protocol in (e), and for the linear protocol in (i). (b),(f),(j) Instantaneous energy spectrum as a function of the normalized time t/t^* for the linear protocol in (b), for the tangential protocol in (f), and for the linear protocol in (j). (c),(g),(k) Fidelity between the ideal final state and the evolved final state versus total transfer time t^* for the linear protocol in (c), for the tangential protocol in (g), and for the linear protocol in (k). (d),(h),(l) Distribution of the gap state during the evolution process for the linear protocol in (d), for the tangential protocol in (h), and for the linear protocol in (l). Fixed total transfer time for the four protocols are set to be $J_0t^* = 1080,\ 676,\ 153,\ 100$, respectively. Other parameters take $L = 21$, $\alpha/\pi = 0.5887$ and $t_{\rm op}/t^* = 0.4923$.

(magenta solid line) in the instantaneous energy spectrum in Fig. 2(b) and modulation of staggered on-site potentials (magenta dotted line) in Fig. 2(a), we identify that the gap state $|\psi_{V_a}\rangle$ evolves along the topological channel in the QST process. This can be strongly reinforced by the distribution of the gap state versus the transfer time as illustrated in Fig. 2(d), in which the state $|\Psi_i\rangle$ initially injected into the interface site is transferred to two end sites with equal probabilities. As noted above, after a finite evolution time, it is hard to achieve an expected QST with $F \approx 1$ due to excessive destruction of the adiabatic criterion. To make a comparison in terms of the speed of QST, we need to set a lower bound of fidelity. To this end, we specify that symmetrical beam splitting is successful when the fidelity is stabilized $\geqslant 0.99$. For the trigonometric protocol, the total transfer time needed for the fidelity reaching 0.99 is $J_0t^* = 1080$, as shown in Fig. 2(c).

To analyze the characteristics of the driving function capable of accelerating the QST process in the symmetrical beam splitter, we continue our analysis by considering a simple example of a linear protocol in which the NN hopping amplitudes changes linearly with time,

$$f(t) = 1 - \frac{2t}{t^*}, \tag{6a}$$

$$J_1 = J_0\left(1 - \frac{t}{t^*}\right), \tag{6b}$$

$$J_2 = J_0\frac{t}{t^*}, \tag{6c}$$

$$V_b = -V_a = J_0\sqrt{\frac{J_2(2t)}{J_0}} = J_0\sqrt{\frac{2t}{t^*}}. \tag{6d}$$

$f(t)$ is modulated to vary continuously from 1 to -1, so symmetrical beam splitting through the topological edge channel is theoretically attainable. Still for the system with size $L = 21$, we plot in Figs. 3(a)–3(d) modulation of the NN hopping amplitudes and staggered on-site potentials for the linear protocol, the corresponding instantaneous energy spectrum as a function of the normalized time, the QST fidelity between the ideal final state and the evolved final state versus the total transfer time, and the distribution of the gap state during the QST process, respectively. For the linear protocol, the total transfer time needed to reach 0.99 fidelity is $J_0t^* = 676$. The improvement of QST efficiency, compared to the trigonometric protocol, can be reasonably explained through analyzing modulation of the driving functions and evolution of the energy gap between the gap state and the adjacent

bulk state. As illustrated in Figs. 3(a) and 2(a), the system is driven at a constant rate during the whole evolution process for the linear protocol, while for the trigonometric protocol the system is mildly driven for a large energy gap at the initial stage of evolution, yet later as the band gap decreases, the driving intensity first increases and then decreases. Therefore, we can conclude that the trigonometric protocol is in the wrong direction of energy spectrum manipulation and hence needs longer total transfer time to achieve high-fidelity QST and suppress nonadiabatic excitations.

In light of the analysis above, to enhance the speed of QST, the driving function should be elaborately designed so that the system can be driven strongly in the case of a large energy gap between the channel and bulk states and mildly in the case of a small energy gap. Next, we consider the scenario of a tangential protocol,

$$f(t) = \frac{\tan\left(\pi t/T_f + \alpha\right)}{\tan\alpha}, \tag{7a}$$

$$J_1 = \frac{J_0}{2}\left(1 + \frac{\tan(\pi t/T_f + \alpha)}{\tan\alpha}\right), \tag{7b}$$

$$J_2 = \frac{J_0}{2}\left(1 - \frac{\tan(\pi t/T_f + \alpha)}{\tan\alpha}\right), \tag{7c}$$

$$-V_a = V_b = J_0\sqrt{\frac{1}{2}\left(1 - \frac{\tan(2\pi t/T_f + \alpha)}{\tan\alpha}\right)}, \tag{7d}$$

where $T_f = \frac{\pi t^*}{2\pi - 2\alpha}$, with free parameter $\alpha \in (\frac{\pi}{2}, \pi)$. The tangential parameter can be fine-tuned for systems of different sizes to increase the efficiency of QST in the symmetrical beam splitter. Through a simple optimization search within the parameter scope, we find that for the system of size $L = 21$, the optimal tangential parameter for the tangential protocol is $\alpha = 0.5887\pi$ and the corresponding transfer time needed to reach 0.99 fidelity is $J_0 t^* = 153$, as demonstrated in Fig. 3(g), which is about 86% shorter than the commonly used trigonometric counterpart. This can be mainly attributed to the fact that for the tangential protocol, the system is strongly driven for a large energy gap at the initial stage of evolution, yet later as the band gap decreases, the driving intensity first decreases and then increases, as depicted in Figs. 3(e)–3(f). Although the beam splitting process can be substantially accelerated through tangential modulation that makes the adiabatic QST contain a small admixture of nonadiabatic character, it is worth noting that the parameter values cannot be taken to the extreme case where the nonadiabaticity is dominant. For example, for the system with size $L = 21$ adopting the tangential protocol with $\alpha = \pi/2 + 0.01$ and $J_0 t^* = 153$, Figs. 4(a)–4(d) demonstrate modulation of the hopping amplitudes and staggered on-site energies for the tangential protocol, the corresponding instantaneous energy spectrum versus the normalized time, the QST fidelity versus the total transfer time, and the distribution of the gap state during the QST process, respectively. The fidelity oscillates strongly and does not reach high values at $J_0 t^* = 153$. In addition, the distribution of gap states at different lattice sites is chaotic during the evolution process, and the system cannot achieve symmetrical beam splitting successfully. This is due to the fact that during most of the evolution process, the

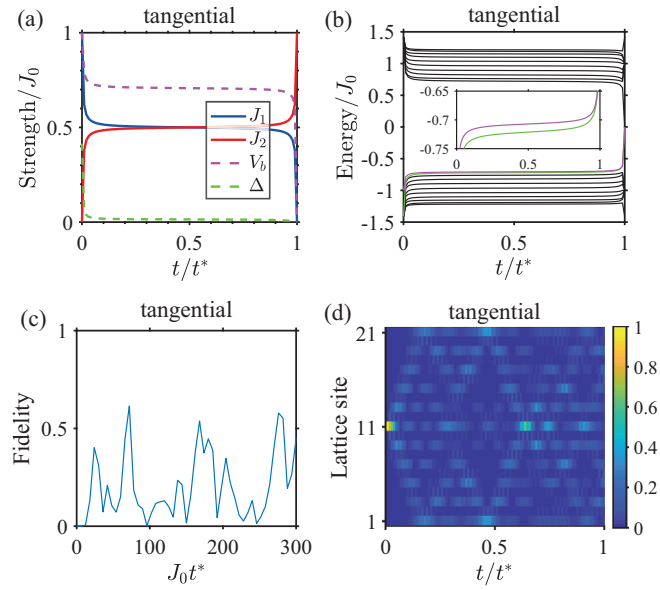

FIG. 4. (a) Evolution of hopping amplitudes and staggered on-site energy (magenta dotted line), as well as the energy gap between the gap state and the adjacent bulk state (green dotted line) for the tangential protocol with $L = 21$, $\alpha = \pi/2 + 0.01$, and $J_0 t^* = 153$. (b) Instantaneous energy spectrum as a function of the normalized time t/t^*. (c) Fidelity of the symmetrical topological beam splitter assisted via edge pumping versus total transfer time t^*. (d) Distribution of the gap state during the evolution process.

channel mode stays at the vicinity of a small band gap, as shown in Fig. 4(b). Thus, the substantial nonadiabatic excitation dynamics between the channel and bulk states leads to destruction of the topology edge channel and failure of symmetrical beam splitting. The common feature of the three modulation schemes mentioned above is that the sum of NN hopping amplitudes $J_1 + J_2$ remains constant throughout the state evolution. In the following, we try to examine whether we could attain a faster QST if such a restriction is lifted. We check this idea by investigating a three-step protocol, in which the evolution process can be divided into three stages: (i) in the first stage, the intracell NN hopping amplitude is kept at the maximum value, while the intercell NN hopping amplitude increases linearly from zero to this value with a larger slope compared to the linear protocol; (ii) in the second stage, the intracell and intercell NN hopping amplitudes remain constant at the maximum value; (iii) in the third stage, the intercell NN coupling strength is kept at the maximum value, while the intracell NN hopping amplitude decreases linearly to zero, i.e.,

$$J_1 = \begin{cases} J_0, & t \leqslant t^* - t_{\rm op} \\ \frac{J_0 t^*}{t_{\rm op}}\left(1 - \frac{t}{t^*}\right), & t > t^* - t_{\rm op}, \end{cases} \tag{8a}$$

$$J_2 = \begin{cases} J_0 \frac{t}{t_{\rm op}}, & t \leqslant t_{\rm op} \\ J_0, & t > t_{\rm op} \end{cases}, \tag{8b}$$

$$V_b = -V_a = J_0\sqrt{\frac{J_2(2t)}{J_0}} = J_0\sqrt{\frac{2t}{t_{\rm op}}}, \tag{8c}$$

as illustrated in Fig. 3(i). The initial and final values of the intracell and intercell NN hopping amplitudes still satisfy the constraints in Eq. (4), so the system can still function as a symmetrical beam splitter when adopting such a three-step modulation protocol. If we keep the mirror symmetry, or in other words, if it is assumed that the time intervals given for the intracell (intercell) NN hopping amplitude to decrease (increase) from initial to final value (and vice versa) is equal, then the only free parameter in the three-step scheme is the time interval $t_{\rm op}$ of a linear increase or decrease. In fact, even if we remove the restriction of mirror symmetry and leave two free parameters for the system adopting either the three-step protocol or the tangential protocol, it can be verified that after parameter optimization, the optimal parameter values will render back the mirror symmetry condition. Through a simple optimization search within the parameter scope, we find that for the system of size $L = 21$, the optimal time of linear increase (decrease) as a proportion of the total transfer time for the three-step protocol is $\beta = t_{\rm op}/t^* = 0.4923$. We plot fidelity between the ideal final state and the evolved final state versus total transfer time t^* for the three-step protocol in Fig. 3(k). The total transfer time required for the fidelity to reach 0.99 is $J_0 t^* = 100$ for the three-step protocol, which is about 90% shorter than the commonly used trigonometric counterpart. As depicted in Fig. 3(j), the instantaneous energy spectrum for the three-step protocol is bent and the mean value of the channel state is significantly increased. As a consequence, the timescales that may be considered inversely proportional to the time average of the eigenenergy of the channel state decrease substantially. We plot the distribution of the gap state versus total transfer time in Fig. 3(l). In accordance with theoretical analysis, the channel mode is localized at the interface site at the beginning instant and localized at two end sites with equal probability at the final instant. As shown by bright fringes in Figs. 3(d), 3(h), and 3(l), the distribution of the topological channel state at odd sites is elongated in the timescale compared with Fig. 2(d), indicating stronger nonadiabatic transitions among the channel state and bulk states under the linear, the tangential, and the three-step driving functions than the commonly used trigonometric counterpart.

C. Optimization of the driving functions

The implementation of fast QST via the topological edge channel in the symmetrical beam splitter is exemplified above in a system of size $L = 21$ with the NN hopping amplitudes and staggered on-site potentials being modulated by the tangential and three-step protocols with fine-tuned tangential and proportional parameters $\alpha = 0.5887\pi$ and $\beta = t_{op}/t^* = 0.4923$, respectively. For different parameter choices in the tangential and three-step modulation schemes, apparent differences in the slopes of the driving functions and the corresponding energy gaps between the gap state and its adjacent bulk state in the instantaneous spectrum will result in different beam splitting effects. In this section, we provide a detailed presentation of the parameter optimization process.

We start our quantitative optimizing procedure with the tangential protocol. As illustrated in Figs. 5(a)–5(d), we investigate fidelity of the symmetrical topological beam splitter

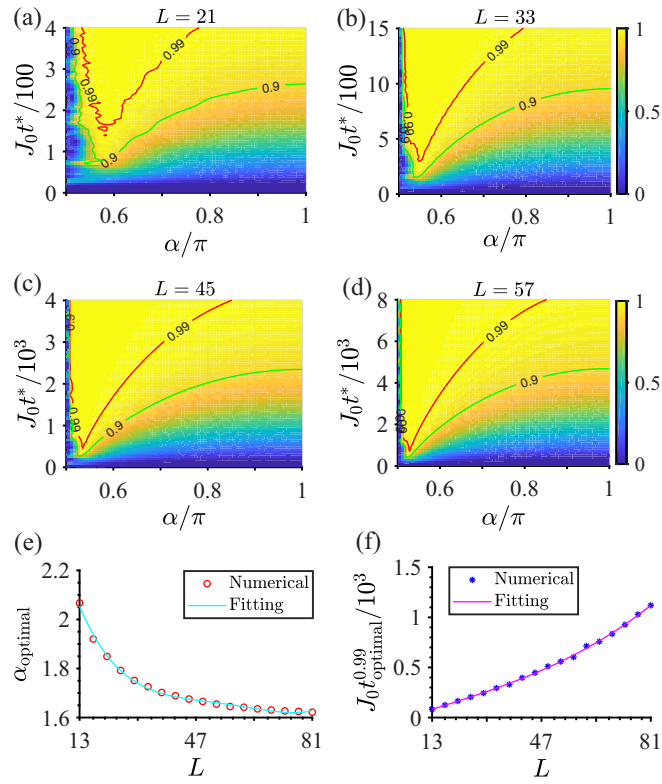

FIG. 5. (a)–(d) Fidelity of the symmetrical topological beam splitter vs the varying α and total transfer time t^* for the tangential protocol with chain size (a) $L = 21$, (b) $L = 33$, (c) $L = 45$, and (d) $L = 57$. The green and red solid lines represent 0.9 and 0.99 fidelity contour lines, respectively. (e),(f) The numerical scatters and fitting functions of optimal tangential parameters in (e) and the corresponding total evolution time needed for 0.99-fidelity in (f) as a function of the size of the chain.

versus the varying α and total transfer time t^* for the tangential protocol with different chain sizes $L = 21$, 33, 45, and 57, respectively. For larger choices of the tangential parameter in the scope $\alpha \in (\frac{\pi}{2}, \pi)$, the total QST duration needed to implement successful symmetrical beam splitting is positively correlated with α, which can be attributed to weakened driving effects in the case of smaller slopes of the modulation functions. However, as noted in Sec. II B, for extremely small choices of the parameter α in the range $(\frac{\pi}{2}, \pi)$, a long stay at the vicinity of the closed energy gap during the evolution process leads to such prominent nonadiabatic excitation between the modes as well as intense oscillations of each mode that the time duration for successful QST through the topological edge channel increases significantly. For a system with fixed size, we can always find a tradeoff point up to which the system can be driven strongly enough to implement the beam splitting function with fast speed, yet gently enough to preserve the topological edge channel and avoid excessive nonadiabatic transition effects. For example, for systems with sizes $L = 21$, 33, 45, and 57, the optimal α for the tangential protocol are $\alpha/\pi = 0.5887$, 0.5493, 0.5333, and 0.5236, respectively. By sampling from chains of different sizes, we plot the optimized tangential parameter and the corresponding evolution timescale needed for 0.99-fidelity QST as functions

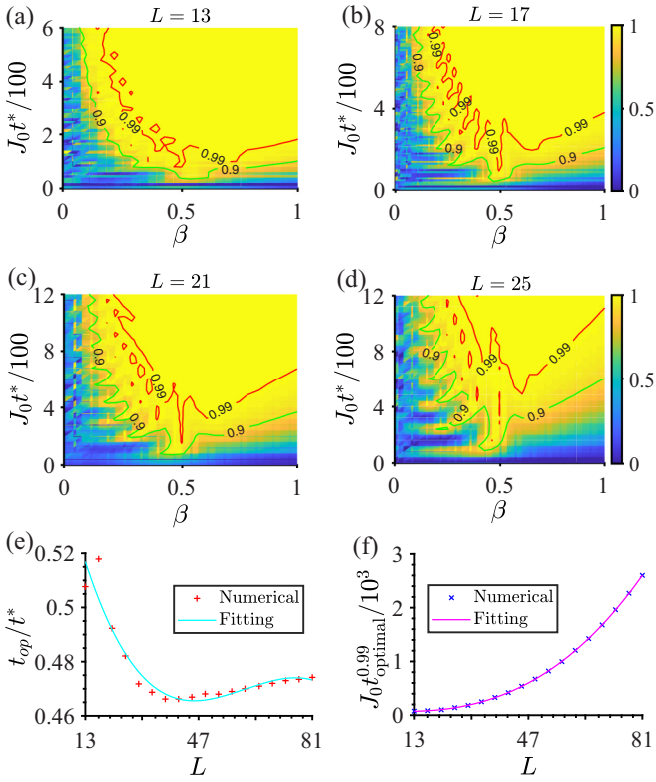

FIG. 6. (a)–(d) Fidelity of the symmetrical topological beam splitter vs the varying β [defined as time interval t_{op} given for the hopping rates to increase (decrease) from the initial to the final value (and vice versa) as a portion of the total transfer time t^*] and total transfer time t^* for the three-step protocol with chain size (a) $L = 13$, (b) $L = 17$, (c) $L = 21$, and (d) $L = 25$. The green and red solid lines represent 0.9 and 0.99 fidelity contour lines, respectively. (e),(f) The numerical scatters and fitting functions of optimal β parameters in (e) and the corresponding total evolution time needed for 0.99-fidelity in (f) as a function of the size of the system.

of chain size in Figs. 5(e) and 5(f). Obviously, the tangential parameter that is negatively correlated to the slope of the driving function decreases with L, and the corresponding transfer time should be large enough to satisfy the adiabatic condition for a longer size of the chain. According to the numerical samples, α_{optimal} versus L and $t^{0.99}_{\text{optimal}}$ versus L can be fitted by a quartic function $\alpha_{\text{optimal}} = 0.0212 \times L^4 - 0.0366 \times L^3 + 0.0131 \times L^2 - 0.041 \times L + 1.6715$ and a cubic function $J_0 t^{0.99}_{\text{optimal}} = 0.0011 \times L^3 - 0.0427 \times L^2 + 10.696 \times L - 52.228$, respectively.

Analogously, for the three-step protocol we plot in Figs. 6(a)–6(d) fidelity of the symmetrical topological beam splitter with different chain sizes $L = 13,\ 17,\ 21,\ 25$ in the parameter space $(\beta,\ t^*)$, in which β is defined as the ratio of time t_{op} for a linear increase (decrease) of the hopping amplitudes to the total transfer time t^*. For larger choices of the proportional parameter in the scope $\beta \in (0, 1)$, the total QST time needed to implement successful symmetrical beam splitting increases with β, which can be explained by its inverse relationship to the slope of the modulation function. However, for smaller choices of β, the 0.9 and 0.99 fidelity contour lines manifest strong oscillations for all values of the total evolution time due to intense nonadiabatic transitions, which are in general undesirable in the QST process since high precision is required when tuning the transfer time. We can always find the optimal parameter β so as to reach a balance between high-efficiency symmetrical beam splitting and avoidance of excessive oscillations. For instance, for systems with sizes $L = 13,\ 17,\ 21,\ 25$ adopting the three-step modulation protocol, the optimal proportional parameters are $\beta = 0.5077,\ 0.5179,\ 0.4923,\ 0.4821$, respectively. As demonstrated in Figs. 6(e) and 6(f), through parameter optimization for systems of different sizes, optimal proportional parameter β_{optimal} versus L as well as corresponding total transfer time $t^{0.99}_{\text{optimal}}$ for the final fidelity reaching 0.99 versus L can be fitted by cubic functions $\beta_{\text{optimal}} = -6.1628 \times 10^{-7} \times L^3 + 0.0001 \times L^2 - 0.0064 \times L + 0.5827$ and $J_0 t^{0.99}_{\text{optimal}} = 0.0032 \times L^3 + 0.1812 \times L^2 - 5.0594 \times L + 101.17$, respectively.

III. DISORDER EFFECT

So far, we have shown several schemes adopting different modulation of the time-dependent NN hopping amplitudes, which allow us to introduce a small admixture of nonadiabatic transitions so as to accelerate the symmetrical beam splitting process, and we provided numerical evidence of high-efficiency QST in the symmetrical beam splitter. Nevertheless, one lingering concern is whether such improvement in QST speed is realized at the cost of performance degradation in other aspects, e.g., robustness against disorders and environmental losses, to name a few. In practical physical systems, due to the existence of erroneous physical implementation and the decoherence effect induced by environmental factors, the modulation of hopping amplitudes and on-site potentials will inevitably deviate from our preset. Therefore, it is necessary to take into account the influence of imperfect factors on the beam splitting process based on these protocols. In the following, we consider the influence of three representative influencing factors: (i) imperfection in hopping amplitudes, which is generally addressed as off-diagonal disorder because it distorts the off-diagonal term of the matrix representation of the Hamiltonian; (ii) defect in on-site potentials, which is generally addressed as diagonal disorder; (iii) losses of on-site potentials due to environment-induced decay. To begin with, we examine the robustness of the four above-mentioned QST protocols by introducing symmetrical disorders both in hopping amplitudes and on-site potentials, and we discuss their effects on the performance of the beam splitter. The way each disorder implementation is imposed on the system parameters can be described by

$$\begin{aligned} J^i_{1(2),n} &\to J^i_{1(2),n}\big(1 + \delta J^i_{1(2)}\big), \\ V^i_{1(2),n} &\to V^i_{1(2),n}\big(1 + \delta V^i_{1(2)}\big), \end{aligned} \tag{9}$$

where the ith pair of samples $\delta J^i_{1(2)}$ and $\delta V^i_{1(2)}$ obtain random real values, uniformly distributed within the range $[-\omega_s,\ \omega_s]$, in which ω_s is termed the disorder strength. $\delta J^i_{1(2)}$ and $\delta V^i_{1(2)}$ are assumed to remain fixed during each evolution process since static disorder is considered here. Without loss of generality, we plot in Fig. 7 the statistical distribution of the transfer fidelity obtained from 10 000 diagonal and off-diagonal

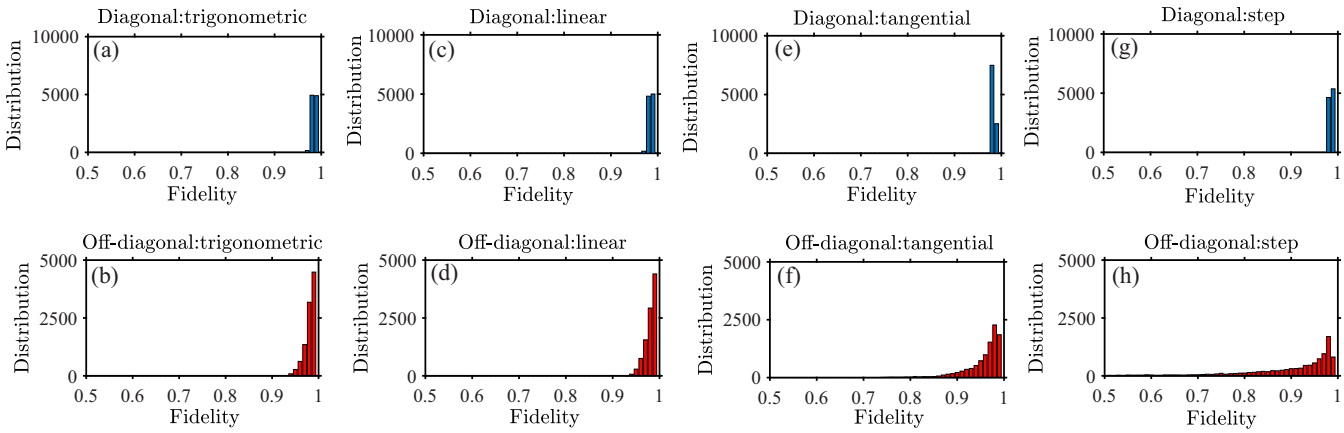

FIG. 7. Robustness against two types of symmetrical disorders for the four protocols. (a),(b) Statistical distribution of fidelity for the trigonometric protocol with total transfer time $J_0t^* = 1080$ under (a) diagonal disorder and (b) off-diagonal disorder. (c),(d) Statistical distribution of fidelity for the linear protocol with total transfer time $J_0t^* = 676$ under (c) diagonal disorder and (d) off-diagonal disorder. (e),(f) Statistical distribution of fidelity for the tangential protocol with total transfer time $J_0t^* = 153$ and $\alpha/\pi = 0.5887$ under (e) diagonal disorder and (f) off-diagonal disorder. (g),(h) Statistical distribution of fidelity for the three-step protocol with total transfer time $J_0t^* = 100$ and $\beta = 0.4923$ under (g) diagonal disorder and (h) off-diagonal disorder. Other parameters take $L = 21$ and $\omega_s = 0.2$.

disorder realizations adopting the trigonometric, linear, tangential, and three-step protocols, respectively, in a symmetrical beam splitter with size $L = 21$ and a moderate disorder strength $\omega_s = 0.2$. Note that the total transfer time for each protocol is fixed to the values when each QST reaches 0.99 fidelity under zero disorder so as to inspect whether the enhancement in efficiency is accompanied by a shortfall of robustness, as calculated in Sec. II B. We can immediately notice that the four protocols exhibit impressively high robustness against diagonal disorder, with their fidelity distributions being concentrated at high values near 0.99. In terms of robustness against off-diagonal disorder, the tangential and three-step protocols obviously underperform their trigonometric and linear counterparts. Such a performance degradation is due to the strong oscillation arising from intense nonadiabatic excitations between the topological channel state and the bulk states. It is no wonder that the improvements in QST efficiency of the tangential and three-step protocols are achieved at the expense of reduced robustness against disorder because of the fast topological pumping induced by nonadiabatic transitions and the large average value of hopping amplitudes for each instant throughout the temporal evolution. Diagonal and off-diagonal disorders as described in Eq. (9) are mirror-symmetric with respect to the topological interface. Next, we will try to reveal the effects of asymmetric disorders. We consider the case of asymmetric distortions on hopping amplitudes and on-site potentials. Their effects on the system parameters can be assumed as

$$J^i_{1(2),n} \to J^i_{1(2),n}\left(1 + \delta J^i_{1(2),L}\right), \quad n = 1, \ldots, \frac{N}{2},$$
$$J^i_{1(2),n} \to J^i_{1(2),n}\left(1 + \delta J^i_{1(2),R}\right), \quad n = \frac{N}{2} + 1, \ldots, N, \quad (10)$$
$$V^i_{1(2),n} \to V^i_{1(2),n}\left(1 + \delta V^i_{1(2),L}\right), \quad n = 1, \ldots, \frac{N}{2},$$
$$V^i_{1(2),n} \to V^i_{1(2),n}\left(1 + \delta V^i_{1(2),R}\right), \quad n = \frac{N}{2} + 1, \ldots, N, \quad (11)$$

where $\delta J^i_{1(2),L(R)}$ and $\delta V^i_{1(2),L(R)}$ acquire random real values from the interval $[-\omega_s, \omega_s]$.

As depicted in Fig. 8, for both kinds of asymmetric disorders for the four protocols with $L = 21$, we plot the average fidelity of the topological beam splitter and phase difference of the evolved final state at two end sites as functions of disorder strength ω_s. The total transfer time for each protocol and chain size is the same as in Fig. 7, so that our system adopting

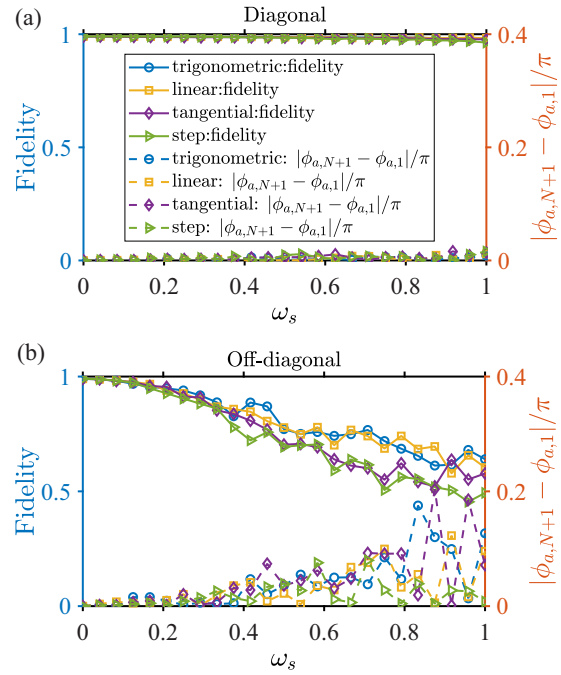

FIG. 8. Average fidelity and phase difference of the evolved final state at two-end sites vs disorder strength for asymmetric (a) diagonal and (b) off-diagonal disorders for the four protocols whose total transfer time is set to be $J_0t^* = 1080$, 676, 153, 100, respectively. Other parameters take $L = 21$, $\alpha/\pi = 0.5887$, and $\beta = 0.4923$.

the four protocols can successfully implement 0.99-fidelity symmetrical beam splitting when disorder strength equals zero. Each point corresponds to the mean value of fidelity $\bar{F} = \frac{1}{M}\sum_{i=1}^{M} F_i$ averaged over $M = 100$ samples for the sake of universality. Numerical results reveal that, when asymmetric diagonal disorders are added into the system, it can almost always function as a symmetrical beam splitter, with insignificant fidelity reduction and phase difference of the evolved final state at the two end sites as ω_s increases. However, in the case of asymmetric off-diagonal disorders, fidelities for the four protocols decrease rapidly with an increase of the disorder strength ω_s. The tangential and three-step protocols manifest weaker robustness against asymmetric off-diagonal disorder than the trigonometric and linear counterparts, as shown in Fig. 8(b). In addition, phase differences of the evolved final state at the two end sites become prominent, and the deviations will be amplified when ω_s increases.

On the other hand, for high-efficiency QST in quantum networks, the systemic loss is another influencing factor. When considering the effect of losses in the lattice chain, the system can be described by the following non-Hermitian Hamiltonian:

$$H' = H - i\sum_n \left[\gamma_n^a a_n^\dagger a_n + \gamma_n^b b_n^\dagger b_n\right], \tag{12}$$

where H is the lossless Hamiltonian given in Eq. (1), and $\gamma_n^{a,b}$ denotes the loss rate of each type of site. For convenience, we assume $\gamma_n^a = \gamma_n^b = \gamma$. The dynamics of the system is governed by the non-Hermitian Liouville equation $\dot{\rho} = -i(H'\rho - \rho H'^\dagger)$. We plot in Fig. 9(a) the final fidelity of QST versus loss rate for a system adopting the four protocols with size $L = 21$. The total transfer time for each protocol is fixed to the values calculated in Sec. II B so that the QST can be successfully implemented via all protocols when no loss exists. Compared with the trigonometric protocol, the fidelities of other protocols have been improved to a different extent, the tangential and three-step protocols in particular, with the degree of improvement depending on their respective total evolution time. We also investigate the performance of different protocols in chains of different sizes, as illustrated in Fig. 9(b). The numerical results indicate that the tangential and three-step protocols manifest a notable amelioration of robustness against environment-induced loss.

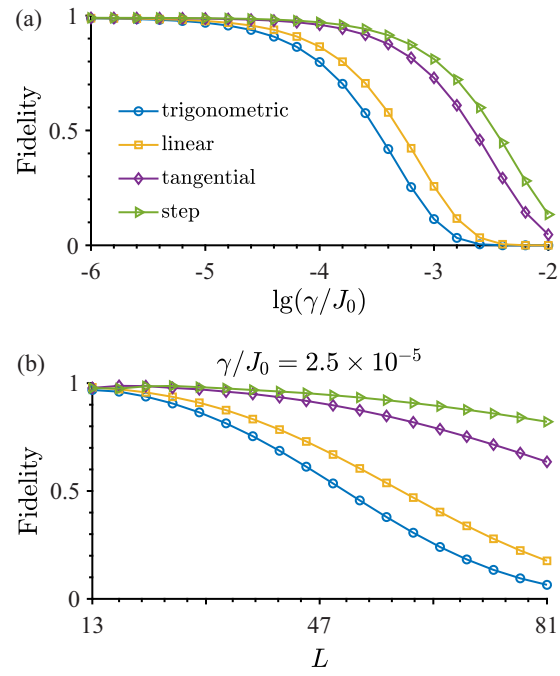

FIG. 9. (a) Final fidelity as a function of loss rate γ for the cosine protocol with $J_0 t^* = 1080$, the linear protocol with $J_0 t^* = 676$, the tangential protocol with $J_0 t^* = 153$ and $\alpha/\pi = 0.5887$, and the three-step protocol with $J_0 t^* = 100$ and $\beta = 0.4923$. (b) Fidelity as a function of the chain size with fixed loss parameter $\gamma = 2.5 \times 10^{-5} J_0$ for the four protocols. Modulation parameters are fixed at the optimal values of $\alpha/\pi = 0.5887$ and $\beta = 0.4923$ for $L = 21$.

IV. SCALABILITY

In the sections above, we have designated effective modulation functions for the hopping amplitudes and on-site potentials in a splicing odd-sized SSH model through engineering a spectrum for substantially speeding up the QST in the symmetrical beam splitter. It has also been proven that the improvement of efficiency comes at the expense of reduced robustness against off-diagonal disorder. In addition, a symmetrical beam splitter adopting the aforementioned protocols exhibits strong robustness against diagonal disorder and improved robustness against environment-induced losses. To obtain a more extensive understanding of the crucial characteristics of a small admixture of nonadiabaticity facilitating QST protocols proposed in this article, another significant property is the scalability. In the following, we examine the performance of the four protocols when the size of the system is altered. We plot in Fig. 10 the total transfer time $t^*_{0.99}$ needed for each protocol to achieve symmetrical beam splitting versus the size of the system, where $t^*_{0.99}$ versus L for the trigonometric, linear, tangential, and three-step

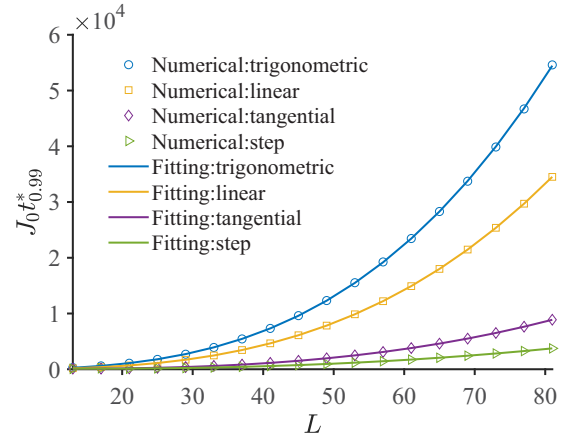

FIG. 10. Numerical results and fitting functions of the total transfer time needed to reach 0.99 fidelity for chains of different sizes for the trigonometric protocol, the linear protocol, the tangential protocol, and the three-step protocol. The parameter α for the tangential protocol and the parameter β for the three-step protocol are set to be the optimal values $\alpha/\pi = 0.5887$, and $\beta = 0.4923$ for the system of size $L = 21$, respectively.

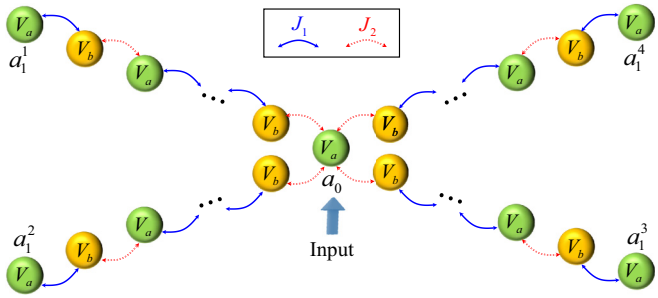

FIG. 11. Schematic illustration of the topological router with four output ports obtained by cross-linking four even-sized SSH chains.

protocols can be fitted by cubic functions $J_0 t_{\text{trig}}^{0.99} = 0.104\,25 \times L^3 - 0.455\,54 \times L^2 + 28.478 \times L - 263.35$, $J_0 t_{\text{lin}}^{0.99} = 0.062\,827 \times L^3 + 0.153\,05 \times L^2 + 1.5217 \times L - 3.3575$, $J_0 t_{\text{tan}}^{0.99} = 0.014\,941 \times L^3 + 0.276\,81 \times L^2 - 13.189 \times L + 184.83$, and $J_0 t_{\text{step}}^{0.99} = 0.002\,95 \times L^3 + 0.520\,58 \times L^2 - 18.431 \times L + 253$, respectively. Obviously, in the symmetrical topological beam splitter modulated by the four protocols, longer total transfer time is needed to realize 0.99-fidelity QST with the augmentation of chain size L. Nevertheless, it is evident that within the range of chain size considered here, the four protocols manifest good scalability, and the efficiency of QST based on the three-step protocol improves most significantly with length, closely followed by the tangential protocol, leaving the trigonometric and linear protocols far behind.

The symmetrical topological beam splitter based on an odd-sized SSH model with staggered on-site potentials and a topological interface is structurally equivalent to the system attained by connecting two even-sized SSH chains with distinct topological order through a mutual additional a-type site. Apart from the size of chains, another important direction for scalability analysis is to investigate the performance of the four protocols when the number of constituent chains in the cross-linking model is altered. We consider a crossed-chain configuration comprised of K identical even-sized SSH chains as depicted in Fig. 11 for the case of $K = 4$. The second-quantized Hamiltonian of the crossed-chain configuration formed by $L = KN + 1$ ($N \in$ even) sites reads

$$H' = \sum_{\sigma}\sum_{n}\left[V_a a_n^{\sigma\dagger} a_n^{\sigma} + V_b b_n^{\sigma\dagger} b_n^{\sigma}\right] + \sum_{\sigma}\sum_{\mathrm{n}=1}^{N/2}\left[J_1 a_n^{\sigma\dagger} b_n^{\sigma} + J_2 a_{n+1}^{\sigma\dagger} b_n^{\sigma} + \mathrm{H.c.}\right], \quad (13)$$

where a_n^{σ} and b_n^{σ} are the annihilation operators of particles at the nth a- and b-type sites in a single SSH chain indexed by σ, respectively, and $a_{N/2+1}^{\sigma} = a_{N/2+1} = a_0$. If we regard the linking site as an input port, and the K end sites as output ports, then the crossed-chain configuration is equivalent to a *topological router* with a tunable number of output ports, in which a particle injected into the linking site can be transferred to K end sites with equal probabilities. Without loss of generality, we take the scenario of $K = 4$ depicted in Fig. 11 as a typical example, and we investigate the performance of

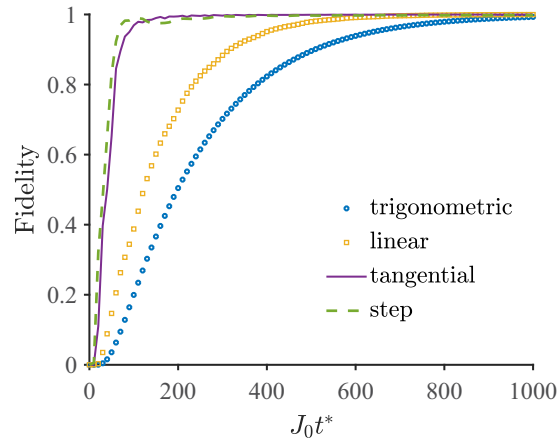

FIG. 12. Final fidelity of the topological router with $K = 4$ output ports as a function of total transfer time for the trigonometric, linear, tangential, and three-step protocols. Other parameters take $L = 4N + 1 = 41$, $\alpha/\pi = 0.5887$, and $\beta = 0.4923$.

the four aforementioned protocols in the following. We plot in Fig. 12 the final fidelity of the topological router with $K = 4$ output ports and $L = 4N + 1 = 41$ as a function of total transfer time for the trigonometric, linear, tangential, and three-step protocols. The parameters in the tangential and three-step protocols are set to be the optimal values in the symmetrical beam splitter with $L = 2N + 1 = 21$. The total transfer time needed for the fidelity to stabilize above 0.99 is $J_0 t^* = 935$ for the trigonometric protocol, $J_0 t^* = 582$ for the linear protocol, $J_0 t^* = 147$ for the tangential protocol, and $J_0 t^* = 266$ for the three-step protocol, respectively. The QST speed for the tangential protocol is still about 84% faster than the commonly used trigonometric counterpart, while the total transfer time needed to realize successful routing for the three-step protocol is only about 72% shorter than the trigonometric counterpart, which is mainly due to the failure of the first peak of the fidelity-t^* curve to reach 0.99. The process of topological routing and the amplitude distribution of the evolved final state under the basis of

$$C = \left(a_1^1, b_1^1, \ldots, a_{N/2}^1, b_{N/2}^1, a_1^2, \ldots, b_{N/2}^2, a_1^3, \ldots, b_{N/2}^3, a_1^4, \times \ldots, b_{N/2}^4, a_{N/2+1}\right)$$

for the four protocols are illustrated in Fig. 13. Apparently, the evolved final state is localized at four end sites in the topological router adopting the four protocols, implying that all protocols can achieve successful topological routing under sufficient transfer time, but the tangential and three-step protocols are obviously faster.

We plot in Fig. 14(a) the total transfer time $t_{0.99}^*$ as a function of the size N of each constituent chain. Obviously, in the topological router with $K = 4$ output ports modulated by the four protocols, longer total transfer time is needed to realize 0.99-fidelity QST with the augmentation of the size N of each constituent chain, which is consistent with the results in the symmetrical beam splitter. In addition, it is evident that within the range of chain size considered here, the four protocols manifest good scalability, and the efficiency of QST based on the three-step protocol improves most significantly with length in general (with a few exceptions in small choices

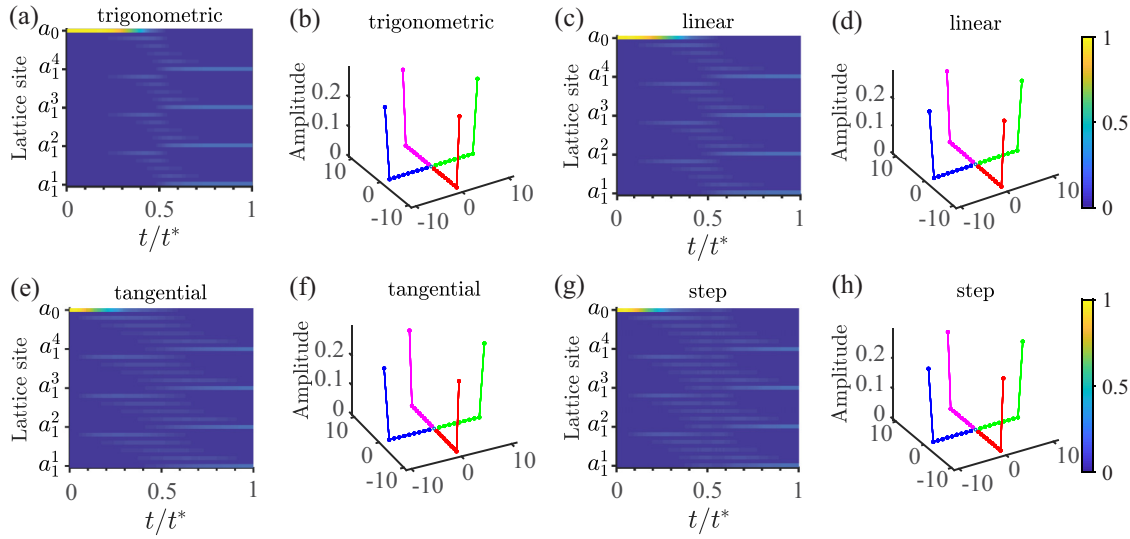

FIG. 13. Distribution of the gap state during the topological routing process and amplitude distribution of the evolved final state for the trigonometric protocol with total transfer time $J_0t^* = 935$ in (a) and (b), for the linear protocol with total transfer time $J_0t^* = 582$ in (c) and (d), for the tangential protocol with total transfer time $J_0t^* = 147$ and $\alpha/\pi = 0.5887$ in (e) and (f), and for the three-step protocol with total transfer time $J_0t^* = 266$ and $\beta = 0.4923$ in (g) and (h).

of N), closely followed by the tangential protocol, leaving the trigonometric and linear protocols far behind.

The total transfer time $t^*_{0.99}$ as a function of the number of constituent chains K is shown in Fig. 14(b), with the size of each constituent chain being fixed at $N = 10$. We can notice that in general, the total transfer time needed to achieve 0.99-fidelity topological routing for the four protocols decreases with the augmentation of the number of constituent chains in the crossed-chain configuration, which can be attributed to a smaller population distribution that needs to be transferred to the end site of each constituent chain in the case of a larger number of chains. However, for the tangential and three-step protocols, this trend in the $t^*_{0.99}$-K curve is broken at several mutation points. For example, for the three-step protocol, $t^*_{0.99}$ increase substantially at $K = 4$; for the tangential protocol, $t^*_{0.99}$ increase substantially at $K = 4$, 10, 15, 19. Such a phenomenon can be attributed to strong oscillation in the F–t^* curves arising from attendance of a small admixture of nonadiabatic transitions in the tangential and three-step protocols as the size of the system $L = KN + 1$ augments rapidly with K, and nonadiabatic excitations do not suffice to achieve high fidelity within a short transfer time. The order of the peak in the F-t^* curve where fidelity reaches 0.99 and stabilizes above this value ever since varies with the size $L = KN + 1$ of the system. Therefore, the tangential and three-step protocols manifest far superior scalability in terms of the size of each constituent chain N to that in terms of the number of constituent chains K in the crossed-chain configuration. But generally, the tangential and three-step protocols exhibit good scalability and outperform the commonly used trigonometric counterpart. This good flexibility provides a broad prospect for applications of topological beam splitters and topological routers in quantum information distribution and large-scale quantum information network construction.

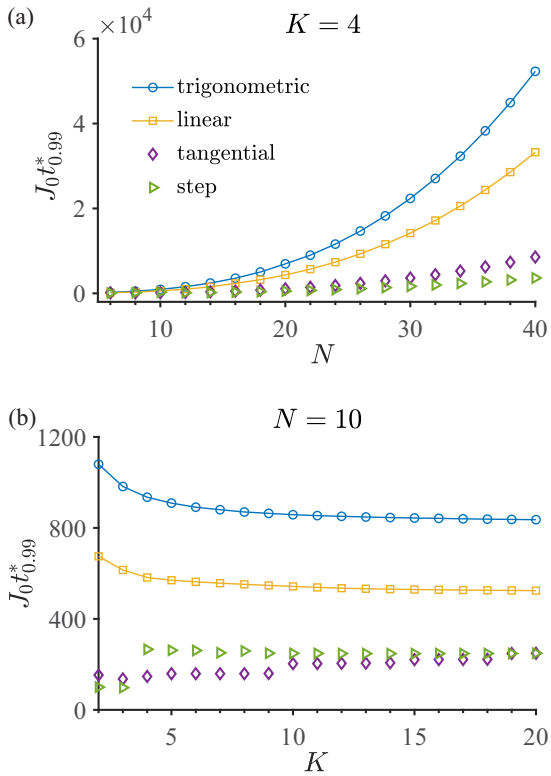

FIG. 14. Total transfer needed to realize 0.99-fidelity QST as a function of (a) the size of each constituent chain with fixed output port number $K = 4$, and (b) the number of output port number with a fixed number of lattice sites in each constituent chain for the four protocols. Other parameters take $\alpha/\pi = 0.5887$ and $\beta = 0.4923$.

V. IMPLEMENTATION OF SPLITTER AND ROUTER MODELS IN QUANTUM OPTOMECHANICAL ARRAYS

As the simplest one-dimensional topological model, the SSH model can be readily constructed in diverse quantum

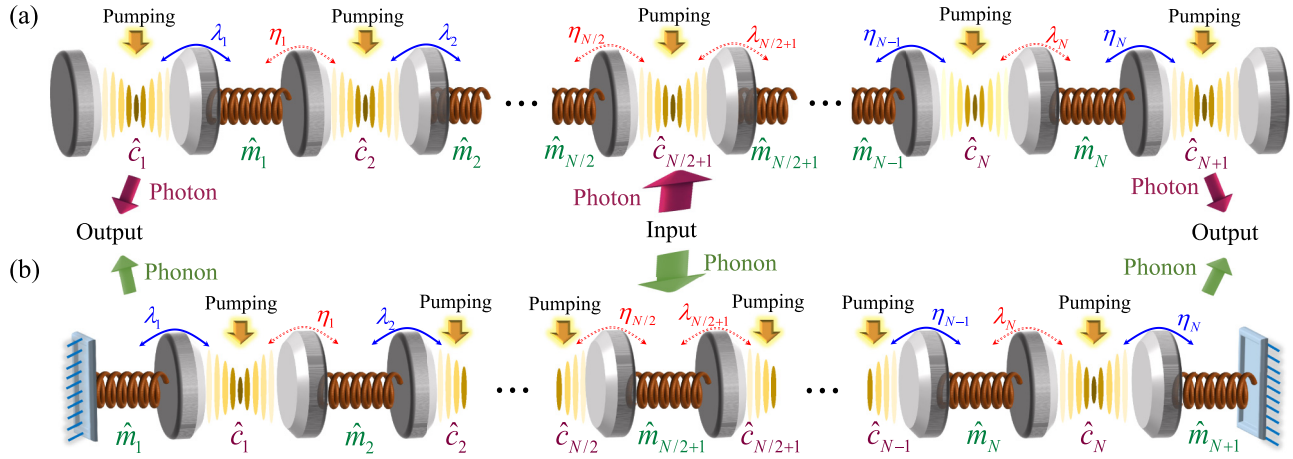

FIG. 15. Schematic of implementing topologically protected (a) photon and (b) phonon splitters in one-dimensional optomechanical arrays with photon and phonon inputs, respectively, at the middle site.

systems [27,28,38–56]. Because the proposed models of splitters and routers in the present work are splicing SSH chains, the SSH model could also be easily implemented in various quantum systems. In this section, we show how to use optomechanical systems to construct the proposed model by alternately assembling optical cavities and mechanical oscillators, enabling topologically protected splitters and routers of photons or phonons.

Taking the implementation of a photon splitter as an example, we consider an alternate assembly of $N+1$ optical cavities and N mechanical oscillators that form a one-dimensional optomechanical array, as shown in Fig. 15(a), where each optical cavity is driven by a pumping laser. Intracell and intercell couplings are realized through the optomechanical radiation pressure with intracell (intercell) coupling strength λ_j (η_j) between the jth mechanical oscillator and the jth [$(j+1)$th] optical cavity. The Hamiltonian of the optomechanical array shown in Fig. 15(a) can be described by

$$H_{\text{total}} = H_0 + H_{\text{om}} + H_{\text{d}}. \tag{14}$$

H_0 is the free Hamiltonian of the optomechanical array

$$H_0 = \sum_{j=1}^{N+1} \omega_{c,j} \hat{c}_j^\dagger \hat{c}_j + \sum_{j=1}^{N} \omega_{m,j} \hat{m}_j^\dagger \hat{m}_j, \tag{15}$$

where $\hat{c}_j^\dagger$ ($\hat{c}_j$) and $\hat{m}_j^\dagger$ ($\hat{m}_j$) are creation (annihilation) operators of the photon and phonon modes in the jth optical cavity and the jth mechanical oscillator, respectively, with corresponding frequencies $\omega_{c,j}$ and $\omega_{m,j}$. The optomechanical radiation pressure coupling is expressed as

$$H_{\text{om}} = -\sum_{j=1}^{N} \left(\lambda_j \hat{c}_j^\dagger \hat{c}_j - \eta_j \hat{c}_{j+1}^\dagger \hat{c}_{j+1}\right)\left(\hat{m}_j^\dagger + \hat{m}_j\right), \tag{16}$$

and H_{d} denotes the laser-pumping interaction with the optical cavities

$$H_{\text{d}} = \sum_{j=1}^{N+1} \left(\Omega_j e^{-i\omega_j t} \hat{c}_j^\dagger + \Omega_j^* e^{i\omega_j t} \hat{c}_j\right), \tag{17}$$

where Ω_j and ω_j represent the amplitude and frequency of the laser driving the jth optical cavity, respectively.

We rotate the frame of the optomechanical array system with respect to the frequency of the laser driving the jth optical cavity by a unitary operator $\exp(-it\sum_j^{N+1} \omega_j \hat{c}_j^\dagger \hat{c}_j)$, and the total Hamiltonian becomes

$$H_{\text{tot}} = \sum_{j=1}^{N+1} \left(\delta_j \hat{c}_j^\dagger \hat{c}_j + \Omega_j \hat{c}_j^\dagger + \Omega_j^* \hat{c}_j\right) + \sum_{j=1}^{N} \left[\omega_{m,j} \hat{m}_j^\dagger \hat{m}_j - \left(\lambda_j \hat{c}_j^\dagger \hat{c}_j - \eta_j \hat{c}_{j+1}^\dagger \hat{c}_{j+1}\right)\left(\hat{m}_j^\dagger + \hat{m}_j\right)\right], \tag{18}$$

where $\delta_j = \omega_{c,j} - \omega_j$ is detuning of the laser driving the jth optical cavity. Assuming the lasers driving optical cavities are strong, we can perform the standard linearization process by rewriting the photon and phonon operators, respectively, as

$$\hat{c}_j = \alpha_j + \hat{a}_j, \quad \hat{m}_j = \beta_j + \hat{b}_j, \tag{19}$$

for which we define the mean $\alpha = \langle \hat{c}_j \rangle$ ($\beta = \langle \hat{m}_j \rangle$) and the fluctuation operator $\hat{a}_j$ ($\hat{b}_j$) of the photon (phonon) annihilation operator $\hat{c}_j$ ($\hat{m}_j$). The linearized Hamiltonian is divided into three parts, $H_{\text{lin}} = H_0' + H_{\text{RW}} + H_{\text{CRW}}$, in which H_0', H_{RW}, and H_{CRW} denote the diagonal term, the rotating-wave term, and the counter-rotating-wave term, respectively, with expressions

$$\begin{aligned} H_0' &= \sum_{j=1}^{N+1} \Delta_j \hat{a}_j^\dagger \hat{a}_j + \sum_{j=1}^{N} \omega_{m,j} \hat{b}_j^\dagger \hat{b}_j, \\ H_{\text{RW}} &= \sum_{j=1}^{N} \left(\lambda_j' \hat{a}_j^\dagger + \eta_j' \hat{a}_{j+1}^\dagger\right) b_j + \text{H.c.}, \\ H_{\text{CRW}} &= \sum_{j=1}^{N} \left(\lambda_j' \hat{a}_j + \eta_j' \hat{a}_{j+1}\right) b_j + \text{H.c.}, \end{aligned} \tag{20}$$

where $\lambda_j' = -\lambda_j \alpha_j$ and $\eta_j' = \eta_j \alpha_{j+1}$ are the effective strengths of optomechanical couplings, and $\Delta_1 = \delta_1 - \lambda_1(\beta_1 + \beta_1^*)$, $\Delta_{j\in[2,N]} = \delta_j - \lambda_j(\beta_j + \beta_j^*) + \eta_j(\beta_{j-1} + \beta_{j-1}^*)$, and $\Delta_{N+1} = \delta_{N+1} + \eta_N(\beta_N + \beta_N^*)$ are effective cavity field detunings.

Under the rotating-wave approximation with conditions $|\Delta_j + \omega_{m,j}| \gg |\lambda'_j|$ and $|\Delta_{j+1} + \omega_{m,j}| \gg |\eta'_j|$, the counter-rotating-wave Hamiltonian $H_{\rm CRW}$ can be neglected, and further performing a rotation operation $\exp\{-it[\sum_j^{N+1}(\Delta - V_a)\hat{a}_j^\dagger \hat{a}_j + \sum_j^N(\omega_m - V_b)\hat{b}_j^\dagger \hat{b}_j]\}$, the effective Hamiltonian of the optomechanical array system can be written as

$$H_{\rm eff} = \sum_{j=1}^{N+1} V_a \hat{a}_j^\dagger \hat{a}_j + \sum_{j=1}^{N} V_b \hat{b}_j^\dagger \hat{b}_j + \left[\sum_{j=1}^{N} \left(\lambda'_j \hat{a}_j^\dagger + \eta'_j \hat{a}_{j+1}^\dagger\right) b_j + \text{H.c.}\right], \tag{21}$$

by setting $\Delta_j = \Delta$, $\omega_{m,j} = \omega_m$, and $\Delta - V_a = \omega_m - V_b$.

The effective Hamiltonian in Eq. (21) can be equivalent to the Hamiltonian of the splitter model in Eq. (1) when setting $\lambda'_j = J_1$ and $\eta'_j = J_2$ for $j \in [1, N/2]$ but $\lambda'_j = J_2$ and $\eta'_j = J_1$ for $j \in [N/2 + 1, N]$, which indicates that the photon splitter model can be constructed by the proposed quantum system of the optomechanical array shown in Fig. 15(a), where the modulation of parameters λ', η'_j, V_a, and V_b in the effective Hamiltonian can be realized by modulating frequencies, amplitudes, and phases of the pumping lasers driving optical cavities [77,78]. In the same way, a phonon splitter can be implemented by the quantum system of the optomechanical array shown in Fig. 15(b), and similarly, topologically protected routers of photons and phonons can also be constructed by splicing more optomechanical chains.

VI. CONCLUSION

To summarize, we have proposed fast and robust symmetrical beam splitters and routers induced by topological edge channel in an odd-sized SSH model with a topological interface and staggered on-site potentials. Several protocols show that a small admixture of nonadiabatic transitions can accelerate the beam splitting process and provide numerical evidence of fast-speed QST in the symmetrical beam splitter. Through parameter optimization, systems of size $L = 21$ adopting the tangential and three-step protocols can realize topologically protected QST from the interface site to two end sites with 0.99 fidelity in timescales that are 86% and 90% shorter than the commonly used trigonometric counterpart, respectively. We prove through numerical sampling that decreased time needed for high-efficiency beam splitting in the tangential and three-step protocols is implemented at the expense of robustness degradation against off-diagonal disorders. Besides, the symmetrical beam splitter adopting the tangential and three-step protocols manifests strong robustness against diagonal disorder and improved robustness against environment-induced losses. In addition, we prove the scalability of the four protocols when the chain size is varied, and we show a crossed-chain configuration to realize a topological router whose number of outports can be conveniently adjusted by cross-linking different numbers of even-sized chains. Finally, we discuss possible implementations of splitters and routers of photon or phonon through constructing optomechanically coupled systems by alternately assembling optical cavities and mechanical oscillators. The fast and robust topological beam splitter via optimizing coupling engineering exhibits sound properties and provides a typical example of functional quantum device, which could trigger further research into efficient quantum information processing and the construction of large-scale quantum networks.

ACKNOWLEDGMENTS

The authors acknowledge the financial support by the National Natural Science Foundation of China (NSFC) (Grants No. 62075048 and No. 12304407), Natural Science Foundation of Shandong Province of China (Grant No. ZR2020MF129), and China Postdoctoral Science Foundation (Grants No. 2023TQ0310 and No. GZC20232446).

[1] P. Král, I. Thanopulos, and M. Shapiro, *Colloquium:* Coherently controlled adiabatic passage, Rev. Mod. Phys. **79**, 53 (2007).

[2] H. Dong, D.-Z. Xu, J.-F. Huang, and C.-P. Sun, Coherent excitation transfer via the dark-state channel in a bionic system, Light Sci. Appl. **1**, e2 (2012).

[3] V. Abramavicius, V. Pranculis, A. Melianas, O. Inganäs, V. Gulbinas, and D. Abramavicius, Role of coherence and delocalization in photo-induced electron transfer at organic interfaces, Sci. Rep. **6**, 32914 (2016).

[4] A. Galindo and M. A. Martín-Delgado, Information and computation: Classical and quantum aspects, Rev. Mod. Phys. **74**, 347 (2002).

[5] N. Gisin and R. Thew, Quantum communication, Nat. Photon. **1**, 165 (2007).

[6] M. Christandl, N. Datta, A. Ekert, and A. J. Landahl, Perfect state transfer in quantum spin networks, Phys. Rev. Lett. **92**, 187902 (2004).

[7] Y.-D. Wang and A. A. Clerk, Using interference for high fidelity quantum state transfer in optomechanics, Phys. Rev. Lett. **108**, 153603 (2012).

[8] S. Tan, R. W. Bomantara, and J. Gong, High-fidelity and long-distance entangled-state transfer with floquet topological edge modes, Phys. Rev. A **102**, 022608 (2020).

[9] A. J. Hoffman, S. J. Srinivasan, J. M. Gambetta, and A. A. Houck, Coherent control of a superconducting qubit with dynamically tunable qubit-cavity coupling, Phys. Rev. B **84**, 184515 (2011).

[10] S. J. Srinivasan, N. M. Sundaresan, D. Sadri, Y. Liu, J. M. Gambetta, T. Yu, S. M. Girvin, and A. A. Houck, Time-reversal symmetrization of spontaneous emission for quantum state transfer, Phys. Rev. A **89**, 033857 (2014).

[11] E. A. Sete, E. Mlinar, and A. N. Korotkov, Robust quantum state transfer using tunable couplers, Phys. Rev. B **91**, 144509 (2015).

[12] A. Kay, Quantum error correction for state transfer in noisy spin chains, Phys. Rev. A **93**, 042320 (2016).
[13] B. Vermersch, P.-O. Guimond, H. Pichler, and P. Zoller, Quantum state transfer via noisy photonic and phononic waveguides, Phys. Rev. Lett. **118**, 133601 (2017).
[14] A. Jayashankar and P. Mandayam, Pretty good state transfer via adaptive quantum error correction, Phys. Rev. A **98**, 052309 (2018).
[15] Y.-D. Wang and A. A. Clerk, Using dark modes for high-fidelity optomechanical quantum state transfer, New J. Phys. **14**, 105010 (2012).
[16] G. D. M. Neto, M. A. de Ponte, and M. H. Y. Moussa, Nonlocal dissipative tunneling for high-fidelity quantum-state transfer between distant parties, Phys. Rev. A **85**, 052303 (2012).
[17] D. J. Thouless, M. Kohmoto, M. P. Nightingale, and M. den Nijs, Quantized hall conductance in a two-dimensional periodic potential, Phys. Rev. Lett. **49**, 405 (1982).
[18] C.-K. Chiu, J. C. Y. Teo, A. P. Schnyder, and S. Ryu, Classification of topological quantum matter with symmetries, Rev. Mod. Phys. **88**, 035005 (2016).
[19] X.-L. Qi and S.-C. Zhang, Topological insulators and superconductors, Rev. Mod. Phys. **83**, 1057 (2011).
[20] A. Bansil, H. Lin, and T. Das, *Colloquium:* Topological band theory, Rev. Mod. Phys. **88**, 021004 (2016).
[21] T. Ozawa, H. M. Price, A. Amo, N. Goldman, M. Hafezi, L. Lu, M. C. Rechtsman, D. Schuster, J. Simon, O. Zilberberg, and I. Carusotto, Topological photonics, Rev. Mod. Phys. **91**, 015006 (2019).
[22] P. Narang, C. A. C. Garcia, and C. Felser, The topology of electronic band structures, Nat. Mater. **20**, 293 (2021).
[23] Y. E. Kraus, Y. Lahini, Z. Ringel, M. Verbin, and O. Zilberberg, Topological states and adiabatic pumping in quasicrystals, Phys. Rev. Lett. **109**, 106402 (2012).
[24] C. Dlaska, B. Vermersch, and P. Zoller, Robust quantum state transfer via topologically protected edge channels in dipolar arrays, Quantum Sci. Technol. **2**, 015001 (2017).
[25] M.-A. Lemonde, V. Peano, P. Rabl, and D. G. Angelakis, Quantum state transfer via acoustic edge states in a 2D optomechanical array, New J. Phys. **21**, 113030 (2019).
[26] J. Cao, W.-X. Cui, X. Yi, and H.-F. Wang, Topological phase transition and topological quantum state transfer in periodically modulated circuit-qed lattice, Ann. Phys. **533**, 2100120 (2021).
[27] L. Qi, G.-L. Wang, S. Liu, S. Zhang, and H.-F. Wang, Controllable photonic and phononic topological state transfers in a small optomechanical lattice, Opt. Lett. **45**, 2018 (2020).
[28] L. Qi, G.-L. Wang, S. Liu, S. Zhang, and H.-F. Wang, Dissipation-induced topological phase transition and periodic-driving-induced photonic topological state transfer in a small optomechanical lattice, Front. Phys. **16**, 12503 (2021).
[29] A. Stern and N. H. Lindner, Topological quantum computation-from basic concepts to first experiments, Science **339**, 1179 (2013).
[30] P. Boross, J. K. Asbóth, G. Széchenyi, L. Oroszlány, and A. Pályi, Poor man's topological quantum gate based on the Su-Schrieffer-Heeger model, Phys. Rev. B **100**, 045414 (2019).
[31] Z.-Z. Li, J. Atalaya, and K. B. Whaley, Topological quantum interference in a pumped Su-Schrieffer-Heeger lattice, Phys. Rev. A **105**, 052418 (2022).
[32] S. Santra, A. Agarwala, and S. Bhattacharjee, Statistics-tuned entanglement of the boundary modes in coupled Su-Schrieffer-Heeger chains, Phys. Rev. B **103**, 195134 (2021).
[33] A. P. Garrido, Á. R. Plastino, M. L. L. de Guevara, and V. M. Apel, Tunable mode entanglement: Topological Su-Schrieffer-Heeger (ssh) chain with an embedded aharonov-bohm quantum ring, Ann. Phys. **534**, 2200201 (2022).
[34] W. P. Su, J. R. Schrieffer, and A. J. Heeger, Solitons in polyacetylene, Phys. Rev. Lett. **42**, 1698 (1979).
[35] E. Fradkin and J. E. Hirsch, Phase diagram of one-dimensional electron-phonon systems. I. The Su-Schrieffer-Heeger model, Phys. Rev. B **27**, 1680 (1983).
[36] E. J. Meier, F. A. An, and B. Gadway, Observation of the topological soliton state in the Su–Schrieffer–Heeger model, Nat. Commun. **7**, 13986 (2016).
[37] Y.-P. Ma and H. Susanto, Topological edge solitons and their stability in a nonlinear Su-Schrieffer-Heeger model, Phys. Rev. E **104**, 054206 (2021).
[38] L. Qi, Y. Xing, S. Liu, S. Zhang, and H.-F. Wang, Topological phase induced by distinguishing parameter regimes in a cavity optomechanical system with multiple mechanical resonators, Phys. Rev. A **101**, 052325 (2020).
[39] J. Cao, W.-X. Cui, X. X. Yi, and H.-F. Wang, Controllable photon-phonon conversion via the topologically protected edge channel in an optomechanical lattice, Phys. Rev. A **103**, 023504 (2021).
[40] X. Z. Hao, X. Y. Zhang, Y. H. Zhou, C. M. Dai, S. C. Hou, and X. X. Yi, Topologically protected optomechanically induced transparency in a one-dimensional optomechanical array, Phys. Rev. A **105**, 013505 (2022).
[41] N. Petropoulos, R. Bogdan Staszewski, D. Leipold, and E. Blokhina, Topological order detection and qubit encoding in Su-Schrieffer-Heeger type quantum dot arrays, J. Appl. Phys. **131**, 074401 (2022).
[42] M. Kiczynski, S. K. Gorman, H. Geng, M. B. Donnelly, Y. Chung, Y. He, J. G. Keizer, and M. Y. Simmons, Engineering topological states in atom-based semiconductor quantum dots, Nature (London) **606**, 694 (2022).
[43] V. D. Pham, Y. Pan, S. C. Erwin, F. von Oppen, K. Kanisawa, and S. Fölsch, Topological states in dimerized quantum-dot chains created by atom manipulation, Phys. Rev. B **105**, 125418 (2022).
[44] F. Bleckmann, Z. Cherpakova, S. Linden, and A. Alberti, Spectral imaging of topological edge states in plasmonic waveguide arrays, Phys. Rev. B **96**, 045417 (2017).
[45] R. S. Savelev and M. A. Gorlach, Topological states in arrays of optical waveguides engineered via mode interference, Phys. Rev. B **102**, 161112(R) (2020).
[46] Y. Yang, Z. Zuo, and D. Cao, Biphoton topology in a quadratic nonlinear waveguide array under the Su-Schrieffer-Heeger model, Phys. Rev. A **104**, 043710 (2021).
[47] A. Coutant, A. Sivadon, L. Zheng, V. Achilleos, O. Richoux, G. Theocharis, and V. Pagneux, Acoustic Su-Schrieffer-Heeger lattice: Direct mapping of acoustic waveguides to the Su-Schrieffer-Heeger model, Phys. Rev. B **103**, 224309 (2021).
[48] Y. Yang and Y. Pan, Engineering zero modes, fano resonance, and tamm surface states in the waveguide-array realization of the modified Su-Schrieffer-Heeger model, Opt. Express **27**, 32900 (2019).

[49] W. Liu, C. Wu, Y. Jia, S. Jia, G. Chen, and F. Chen, Observation of edge-to-edge topological transport in a photonic lattice, Phys. Rev. A **105**, L061502 (2022).

[50] C. Wu, W. Liu, Y. Jia, G. Chen, and F. Chen, Observation of topological pumping of a defect state in a fock photonic lattice, Phys. Rev. A **107**, 033501 (2023).

[51] G. Engelhardt, M. Benito, G. Platero, and T. Brandes, Topologically enforced bifurcations in superconducting circuits, Phys. Rev. Lett. **118**, 197702 (2017).

[52] F. Mei, G. Chen, L. Tian, S.-L. Zhu, and S. Jia, Robust quantum state transfer via topological edge states in superconducting qubit chains, Phys. Rev. A **98**, 012331 (2018).

[53] X. Li, Y. Ma, J. Han, T. Chen, Y. Xu, W. Cai, H. Wang, Y. P. Song, Z.-Y. Xue, Z.-q. Yin, and L. Sun, Perfect quantum state transfer in a superconducting qubit chain with parametrically tunable couplings, Phys. Rev. Appl. **10**, 054009 (2018).

[54] X.-L. Yu, L. Jiang, Y.-M. Quan, T. Wu, Y. Chen, L.-J. Zou, and J. Wu, Topological phase transitions, majorana modes, and quantum simulation of the Su–Schrieffer–Heeger model with nearest-neighbor interactions, Phys. Rev. B **101**, 045422 (2020).

[55] M. Esmann, F. R. Lamberti, A. Lemaître, and N. D. Lanzillotti-Kimura, Topological acoustics in coupled nanocavity arrays, Phys. Rev. B **98**, 161109(R) (2018).

[56] L.-S. Zeng, Y.-X. Shen, Y.-G. Peng, D.-G. Zhao, and X.-F. Zhu, Selective topological pumping for robust, efficient, and asymmetric sound energy transfer in a dynamically coupled cavity chain, Phys. Rev. Appl. **15**, 064018 (2021).

[57] X. Li, Y. Meng, X. Wu, S. Yan, Y. Huang, S. Wang, and W. Wen, Su-Schrieffer-Heeger model inspired acoustic interface states and edge states, Appl. Phys. Lett. **113**, 203501 (2018).

[58] C. Yuce and H. Ramezani, Topological states in a non-hermitian two-dimensional Su-Schrieffer-Heeger model, Phys. Rev. A **100**, 032102 (2019).

[59] D. Obana, F. Liu, and K. Wakabayashi, Topological edge states in the Su-Schrieffer-Heeger model, Phys. Rev. B **100**, 075437 (2019).

[60] M. Kim and J. Rho, Topological edge and corner states in a two-dimensional photonic Su-Schrieffer-Heeger lattice, Nanophotonics **9**, 3227 (2020).

[61] K. Xu, X. Zhang, K. Luo, R. Yu, D. Li, and H. Zhang, Coexistence of topological edge states and skin effects in the non-hermitian Su-Schrieffer-Heeger model with long-range nonreciprocal hopping in topoelectric realizations, Phys. Rev. B **103**, 125411 (2021).

[62] A. F. Tzortzakakis, A. Katsaris, N. E. Palaiodimopoulos, P. A. Kalozoumis, G. Theocharis, F. K. Diakonos, and D. Petrosyan, Topological edge states of the $\mathcal{PT}$-symmetric Su-Schrieffer-Heeger model: An effective two-state description, Phys. Rev. A **106**, 023513 (2022).

[63] L. Qi, G.-L. Wang, S. Liu, S. Zhang, and H.-F. Wang, Engineering the topological state transfer and topological beam splitter in an even-sized Su-Schrieffer-Heeger chain, Phys. Rev. A **102**, 022404 (2020).

[64] L. Qi, Y. Xing, X.-D. Zhao, S. Liu, S. Zhang, S. Hu, and H.-F. Wang, Topological beam splitter via defect-induced edge channel in the rice-mele model, Phys. Rev. B **103**, 085129 (2021).

[65] L. Qi, Y. Yan, Y. Xing, X.-D. Zhao, S. Liu, W.-X. Cui, X. Han, S. Zhang, and H.-F. Wang, Topological router induced via long-range hopping in a Su-Schrieffer-Heeger chain, Phys. Rev. Res. **3**, 023037 (2021).

[66] L.-N. Zheng, X. Yi, and H.-F. Wang, Engineering a phase-robust topological router in a dimerized superconducting-circuit lattice with long-range hopping and chiral symmetry, Phys. Rev. Appl. **18**, 054037 (2022).

[67] K. L. Zhang, P. Wang, and Z. Song, Exceptional-point-induced lasing dynamics in a non-hermitian Su-Schrieffer-Heeger model, Phys. Rev. A **99**, 042111 (2019).

[68] P. M. Gunnink, B. Flebus, H. M. Hurst, and R. A. Duine, Nonlinear dynamics of the non-hermitian Su-Schrieffer-Heeger model, Phys. Rev. B **105**, 104433 (2022).

[69] H. Li, R. Yao, B. Zheng, S. An, M. Haerinia, J. Ding, C.-S. Lee, H. Zhang, and W. Guo, Electrically tunable and reconfigurable topological edge state laser, Optics **3**, 107 (2022).

[70] M.-S. Wei, M.-J. Liao, C. Wang, C. Zhu, Y. Yang, and J. Xu, Topological laser with higher-order corner states in the 2-dimensional Su-Schrieffer-Heeger model, Opt. Express **31**, 3427 (2023).

[71] M. Ezawa, N. Ishida, Y. Ota, and S. Iwamoto, Supersymmetric non-hermitian topological interface laser, Phys. Rev. B **107**, 085302 (2023).

[72] S. Longhi, Topological pumping of edge states via adiabatic passage, Phys. Rev. B **99**, 155150 (2019).

[73] F. M. D'Angelis, F. A. Pinheiro, D. Guéry-Odelin, S. Longhi, and F. Impens, Fast and robust quantum state transfer in a topological Su-Schrieffer-Heeger chain with next-to-nearest-neighbor interactions, Phys. Rev. Res. **2**, 033475 (2020).

[74] I. Brouzos, I. Kiorpelidis, F. K. Diakonos, and G. Theocharis, Fast, robust, and amplified transfer of topological edge modes on a time-varying mechanical chain, Phys. Rev. B **102**, 174312 (2020).

[75] N. E. Palaiodimopoulos, I. Brouzos, F. K. Diakonos, and G. Theocharis, Fast and robust quantum state transfer via a topological chain, Phys. Rev. A **103**, 052409 (2021).

[76] L. Huang, Z. Tan, H. Zhong, and B. Zhu, Fast and robust quantum state transfer assisted by zero-energy interface states in a splicing Su-Schrieffer-Heeger chain, Phys. Rev. A **106**, 022419 (2022).

[77] A. Mari and J. Eisert, Gently modulating optomechanical systems, Phys. Rev. Lett. **103**, 213603 (2009).

[78] C.-H. Bai, D.-Y. Wang, S. Zhang, S. Liu, and H.-F. Wang, Strong mechanical squeezing in a standard optomechanical system by pump modulation, Phys. Rev. A **101**, 053836 (2020).